PNAS NEXUS

PNAS Nexus, 2025, 4, pgaf108
https://doi.org/10.1093/pnasnexus/pgaf108
Advance access publication 8 April 2025
Research Report

Raman investigation of in vivo radiation exposure on melanin in murine hair

Monika Poonia[a], Spencer A. Witte[a], Mallard Woodward[a], Prasant Yadav[b], Sapna Puri[b], Ramasamy Santhanam[b], Naduparambil K. Jacob[b,c] and Zachary D. Schultz[a,c,*]

[a]Department of Chemistry and Biochemistry, The Ohio State University, Columbus, OH 43210, USA
[b]Department of Radiation Oncology, College of Medicine, The Ohio State University, Columbus, OH 43210, USA
[c]Comprehensive Cancer Center, The Ohio State University, Columbus, OH 43210, USA
*To whom correspondence should be addressed: Email: schultz.133@osu.edu
Edited By Levi Thompson

Abstract

Determining the effects of ionizing radiation from unintended exposure in a nuclear event requires the identification of relevant biomarkers and development of methods to retrospectively estimate the absorbed dose. Melanin, a biologically important natural pigment found in hair, shows promise as a biomarker to assess potential radiation exposure. We investigated Raman spectroscopy as a rapid and noninvasive technique to assess changes in melanin from the hair of C57BL/6 mice to gamma radiation between 0 and 4 Gy. Two excitation wavelengths (532 and 785 nm) were employed to probe the melanin response for changes with radiation exposure. Excitation wavelength-dependent variation in Raman features indicates resonance Raman effects, where a 785-nm excitation is more sensitive to the effects of gamma radiation. Melanin-specific Raman features were identified as potential biomarkers for gamma-radiation exposure and used to distinguish between irradiated and nonirradiated mice. Partial least square discriminant analysis models of exposure exhibited enhanced sensitivity to irradiation at 785 nm excitation and yielded a sensitivity of 88% and a specificity of 83%. Mice were classified with 100% sensitivity and specificity up to day 7 at a known time point. A decline in specificity and classification accuracy correlated with alterations in melanin's spectra after >7 days following irradiation. Regression models of the Raman spectrum determined the exposed dose with a precision of <1 Gy at a known exposure time point. This noninvasive approach offers promising applications in radiation biodosimetry and medical monitoring, providing retrospective detection of gamma-radiation exposure at clinically relevant doses.

Keywords: melanin, radiation exposure, Raman spectroscopy, machine learning, biodosimetry

Significance Statement

Changes in the Raman spectra of melanin from the hair from gamma-irradiated mice can be modeled for exposure in a rapid and noninvasive manner. The specific melanin chromophore measured is shown to impact the dosimetry results. Using the Raman spectra as inputs for machine learning models, radiation exposure was classified with 100% accuracy 1 day following exposure.

Introduction

Melanin, a complex biopolymer, plays a crucial role in various biological processes and is primarily responsible for the pigmentation of skin and hair. There are several types of melanin, including eumelanin, pheomelanin, neuromelanin, allomelanin, and pyomelanin, each with distinct chemical compositions and properties (1). Among these, eumelanin—a large biopolymer composed of 5,6-dihydroxyindole and 5,6-dihydroxyindole-2-carboxylic acid—is the most prevalent melanin in human tissues, producing brown-to-black pigments, and acts similarly as sunscreen by providing protection from solar radiation (2–5). Melanins are complex heterogeneous polymers made up of various subunits and cross-linked structures. Work on synthetic melanins has shown the emergence of melanin-like properties from smaller subunits (6). Despite extensive studies, a complete atomic-level model of melanin's structure remains elusive and is a subject for further investigation.

The response of melanin to ionizing radiation exposure, particularly at low doses, has gained significant interest in recent years due to its potential implications for radiation protection and biological dosimetry. Melanocytes, the cells responsible for melanin production, play a crucial role in radiation protection and are potential sites of radiation-induced damage (7–10). Ionizing radiation exposure, originating from both natural cosmic sources and artificial sources like medical procedures or

Competing Interest: N.K.J. is a co-founder and a consultant for Capture Collective Inc., Columbus, OH, USA. Z.D.S., N.K.J., and S.A.W. are co-inventors of patent PCT/US2023/027747.
Received: November 22, 2024. **Accepted:** March 25, 2025

occupational settings, can induce various structural and chemical changes in melanin. These changes in melanin could have significant implications for our understanding of radiation damage and protection mechanisms (11–13). Low-dose radiation has been observed to increase melanin-derived radicals in mouse skin, suggesting a potential adaptive response (8). These melanin-derived radicals in skin can be an endogenous marker for low-dose irradiation, indicating that changes in melanin can potentially be used to detect radiation exposure and retrospective measurement of the absorbed dose. Exposure to ionizing radiation alters the electronic properties of melanin and enhances the electron transfer capabilities of melanin as demonstrated by changes in its electron spin resonance signal (14). Further, melanin acts as a natural radioprotector in organisms exposed to gamma radiation (15). Its complex polymer structure allows it to absorb and dissipate the energy from ionizing radiation, reducing damage to cellular components (15). Gamma rays interact with melanin to change its oxidation–reduction behavior, and redox cycling capacity is enhanced when a reductant is present, which can result in electric current production. Gamma rays appear to excite electrons in melanin molecules, potentially initiating processes that could produce chemical energy for the cell. This mechanism has been compared with photosynthesis, suggesting melanin might collect energy from various types of radiation (16). However, the analysis of radiation-induced changes to melanin is complicated by its complex structure and the presence of various chromophores (1). These chromophores, which are responsible for melanin's broad, featureless light-absorbing properties (17, 18), may exhibit different responses to radiation depending on their specific chemical environment. This complexity necessitates the development of rapid and accurate noninvasive analytical methods to fully characterize the effects of radiation on melanin and detect biochemical changes in individuals.

Raman spectroscopy has emerged as a powerful, noninvasive technique for analyzing the chemical composition and structure of biological materials, including melanin (19–24). This technique relies on the inelastic scattering of monochromatic light to provide a unique spectral fingerprint of the sample (25). Raman spectroscopy allows for nondestructive and high-resolution analysis, offering a novel approach to understanding structural alterations in carbon-rich materials like hair (26, 27). Raman signals of in vivo cutaneous melanin are consistent with those observed in natural and synthetic eumelanin (28). Several studies have explored the use of Raman spectroscopy as a noninvasive technique to characterize melanin and evaluate radiation-induced changes in melanin (19, 20, 29–32). Lam et al. (30) have investigated in vitro ^{60}Co gamma-ray exposure to female human black hair by Raman spectroscopy, and dose-dependent defects were shown, more prominent at doses >10 Gy.

In this study, we investigated the impact of gamma irradiation on hair melanin within C57BL/6 mice using Raman spectroscopy with 532 and 785 nm excitation wavelengths. Animal models, particularly C57BL/6 mice, with their predominantly dark fur, serve as an ideal model for investigating these radiation-induced melanin alterations (33). While multiple types exist, eumelanin is the primary form found in C57BL/6 mice hair (34). Eumelanin shows strong photoprotective properties, and its presence in the hair makes it an important element in assessing radiation exposure and its biological effects (4, 10, 35, 36). Raman spectroscopy enables nondestructive analysis of its structure in hair samples (37). The Raman spectra of melanin exhibited a strong dependence on the excitation wavelength. Notably, our findings suggest that the 785 nm wavelength is more sensitive than 532 nm to the subtle effects of radiation on melanin, which is related to the distinct spectral variation in melanin with excitation wavelength. We identified several melanin features in the Raman spectra that were sensitive to gamma rays, potentially serving as biomarkers. The Raman biomarkers incorporated with machine learning algorithms were used to distinguish between healthy mice and those exposed to gamma radiation. A significant aspect of our study was the investigation of time-dependent changes in melanin spectra following radiation exposure. The observed spectral changes may correlate with physiological repair mechanisms or progressive damage accumulation within the melanin pigment over time. These Raman biomarkers, coupled with machine learning techniques, represent a significant advance in radiation exposure detection and measuring the absorbed dose. The ability of these biomarkers to provide both early and persistent detection of gamma-radiation exposure at clinically relevant doses offers promise for applications in radiation protection and medical monitoring.

Materials and methods

Materials

Acetaminophen powder was purchased from Sigma-Aldrich and was used as received. Absolute ethanol was purchased from Decon Labs for cleaning purposes. Commercial glass microscope slides (Globe Scientific Inc.) were coated with a 50-nm thick layer of gold (Au, American Elements, 99.999%) using a thermal evaporation deposition system (Kurt J. Lesker Company), to reduce glass interference during Raman measurements.

Animals

Mice studies were performed following compliance with the guidelines approved by the Institutional Animal Care and Use Committee of The Ohio State University (OSU) (protocol #2011A00000029-R4). In this study, 10-week-old adult male and female mice, *Mus musculus* (C57BL/6; Cat #000664), were purchased from The Jackson Laboratory and were acclimatized for 1 week before the exposure to gamma rays. All mice were maintained under a 12-h light/dark cycle with standard rodent chow and water ad libitum.

Gamma-radiation exposure

The young adult male and female mice were arranged according to gender and were placed in a RadDisk (Braintree Scientific Inc.) for total body irradiation using a Gammacell 40 Exactor (^{137}Cs source, Best Theratronics). The nonanesthetized animals were exposed to the varying dosages of gamma radiation of 1, 2, and 4 Gy at a conventional dose rate (~0.8 Gy/min), and sham-exposed animals were used as controls. Each dose group (0, 1, 2, and 4 Gy) had four biological replicates (individual mice) for both males and females. The dosimetry of the Gammacell 40 exactor was done annually by Best Theratronics using the Fricke dosimetry system.

Sample collection

Hair samples were collected from anesthetized mice at multiple early time points, including days 1, 7, and 25 postirradiation. The animals were tagged and followed longitudinally following irradiation. Hair was collected from the animals by holding in one hand by the tail, and multiple tufts of hair were plucked from the neck area and upper dorsal body using forceps under sterile conditions. The hair samples were collected into multiple safe-lock Eppendorf tubes—at different time points and snap frozen

immediately using liquid nitrogen, followed by storage at −80 °C until further processing.

Raman sample preparation

Hair samples were removed from the −80 °C freezer at least 30 min prior to the measurement to allow thawing. No chemical alterations were made to the hair samples. Once thawed, a small sample of hairs was carefully pulled out from the tube, and 5–10 strands were placed straight onto double-sided tape on a pre-cleaned gold-coated glass microscope slide. The double-sided tape ensures the hairs lie flat for Raman measurements. Gold slides were thoroughly rinsed with absolute ethanol and dried with a lint-free Kimwipe before placing a fresh piece of double-sided tape for each new sample. Figure S1 shows the intact hair strands on the glass slide together with white light images of the root bulb, shaft, and the tip of the hair under the microscope.

Raman instrumentation and spectral measurements

Raman spectra were acquired using a Renishaw inVia Qontor (Renishaw plc.) spectrometer. The measurements were performed using excitation wavelengths of 532 and 785 nm with a grating of 1,800 and 1,200 lines/mm, respectively. Both laser sources were allowed to warm up for at least 30 min for stability, and laser power was measured with a Thorlabs S130C slim power sensor. Laser light was focused on samples through a Leica N PLAN, 50× long working distance objective (0.5 NA). Prior to spectral measurements, optics were aligned, and the Raman spectrum of acetaminophen powder was collected each day to check the calibration of the spectrometer.

Hair sample measurements were performed by focusing the laser beam on the midpoint of the hair shaft, typically located between 3,000 and 4,500 µm from the root bulb, depending on the length of the hair. Laser power at the sample was ∼0.1 and ∼0.7 mW for 532 and 785 nm, respectively. Raman spectra were acquired in the wavenumber range of 200–3,200 cm^{-1} with an acquisition time of 10 s. White light images were acquired before and after spectral acquisition with the inVia sample-view camera to ensure the hair sample was not damaged by the laser. Three technical replicate spectra were collected for each of four biological replicates (mice), making a total of 12 spectra per dose group. A total of $n = 144$ measurements were taken from 48 male and female mice at a 532-nm excitation wavelength with 0 and 4 Gy for days 1, 7, and 25 postexposure. A similar set of spectral data was acquired from the same animals using a 785-nm excitation source.

Spectral processing

All data analysis was performed in MATLAB (MATLAB R2022a; The MathWorks, Inc.). Prior to preprocessing the raw spectra cosmic rays were removed from each spectrum in WiRE 5 using the width of features algorithm. All spectra were baseline corrected using a rolling circle filter background subtraction code (38) with a radius of 1,000,000 and further normalized to the maximum intensity. Gaussian fitting analysis was performed with Peakfit 9.0 (MATLAB program) to extract intensity, width, and area from melanin spectra acquired at both excitation wavelengths. Second derivatives were performed using Savitzky–Golay filter (39) (ddx = 2, $N = 2$, $F = 35$). All spectra were trimmed from 400 to 1,800 cm^{-1} region and smoothed using a Savitzky–Golay filter (ddx = 0, $N = 2$, $F = 51$) for noise reduction in analysis.

Prediction and classification analysis

Partial least squares regression (PLSR) and partial least squares discriminant analysis (PLS-DA) models were constructed in MATLAB with PLS_Toolbox 8.7.1 (Eigenvector Research, Inc., Manson, WA, USA). Second derivative spectra within the 400–1,800 cm^{-1} range were used as input features, and sample-level prediction and classification were acquired for both 532 and 785 nm datasets independently. To create a robust prediction model that accounts for potential gender differences in melanin response to radiation, both male and female spectral data were combined for unirradiated and gamma-irradiated mice across all time points. To reduce potential biological variability, technical replicate spectra were averaged to produce a single spectrum per animal. Variable importance in projection (VIP) analysis was executed to identify the spectral variables contributing significantly to prediction. To identify the most important spectral features and improve the model's interpretation an automated variable selection utilizing selectivity ratio and VIP scores was performed in PLS toolbox. A regression model was then developed to estimate the time since exposure. Further, spectral data were split into unirradiated and gamma-irradiated groups to develop a triage model using PLS-DA. To evaluate the model's classification performance, the area under the receiver operating characteristic (ROC) curve was generated. The performance of the models constructed with the selected variables was compared with the original models using the R^2 and root mean square error (RMSE) values. Model performance was evaluated using leave-one-out (LOO) and venetian blind (VB) cross-validation methods. The optimal number of latent variables (LVs) for each model was used as per the model suggestions, based on the appropriate RMSE value for cross-validation.

Results

Melanin features at 532 and 785 nm

Raw melanin spectra from $n = 144$ measurements of unirradiated and gamma-irradiated hair samples at 532 and 785 nm are shown in Fig. 1. Melanin spectra acquired at 532 nm exhibit prominent D and G bands at 1,411 and 1,602 cm^{-1}, respectively (Fig. 1A). Both D and G bands associated with melanin exhibit broad peaks with a red shift in frequencies when excited with a 785-nm laser, appearing at ∼1,400 ± 30 and 1,539 ± 50 cm^{-1}, respectively (Fig. 1B). These bands are consistent with previously reported eumelanin Raman spectra within human hair and other biological samples (19, 28, 30). Figure 1C represents a comparative analysis of normalized mean spectra of melanin acquired at both excitation wavelengths, showing significant differences in the peak positions and widths of the spectral features. The intensity ratio I_D/I_G exhibits an increase from 0.59 to 0.87 upon measurement at a wavelength of 785 nm. As a complex biopolymer with various chromophores, melanin likely contains components that resonate more strongly with one laser wavelength than another.

The observed broadening of two Raman bands at higher excitation wavelengths suggests that the spectra were a superimposition of two or more underlying signals, likely originating from different molecular components associated with similar vibrational modes (28). A peak fit model was therefore used to deconvolute the melanin spectra as shown in Fig. 1C. Raman spectra for both 532 and 785 nm excitation were deconvoluted using Gaussian peak shapes with a linear baseline correction (Fig. S2A and B). The peak positions, intensities, full widths, and integrated areas of all peaks were extracted from the resulting curve fits, and

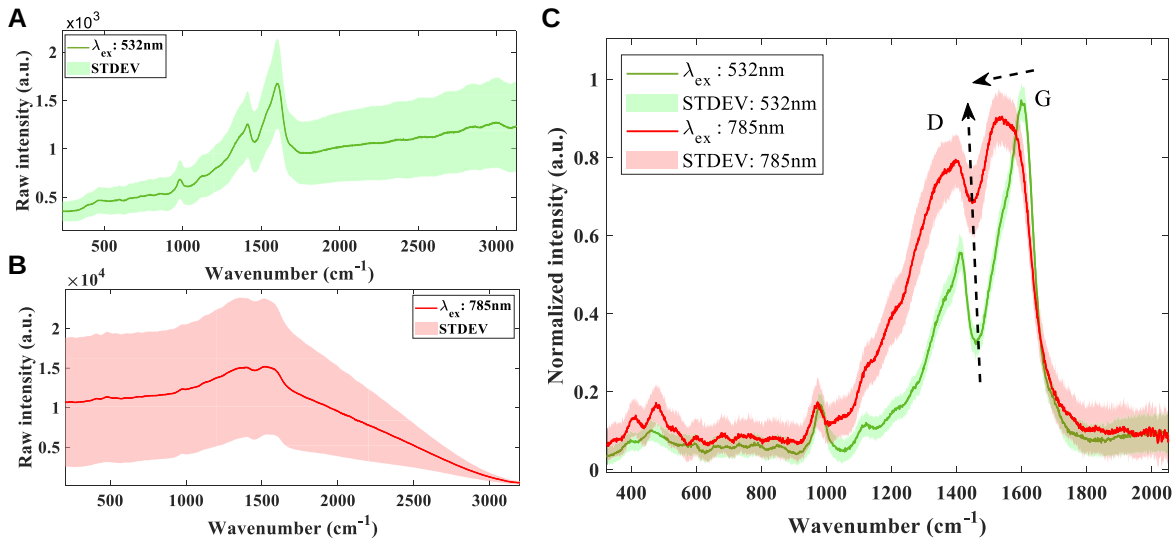

Fig. 1. Mean raw spectra of melanin ($n = 144$) measured from unirradiated and gamma-irradiated hair samples at the laser wavelengths of 532 nm (A) and 785 nm (B). Comparison of mean Raman spectrum at both excitation wavelengths after baseline correction and normalization (C). The shaded part refers to the standard deviation (STDEV) of the spectrum. The changes in the melanin spectrum with increasing wavelength are indicated by arrows.

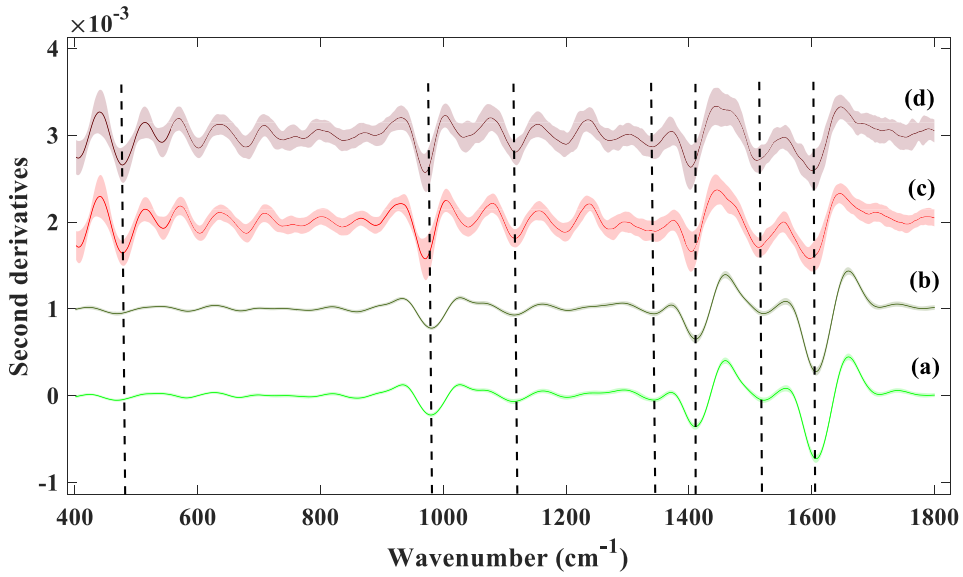

Fig. 2. Mean second derivative spectra of melanin (400–1,800 cm^{-1}) acquired at 532 nm for (a) 0 Gy and (b) 4 Gy, and at 785 nm for (c) 0 Gy and (d) 4 Gy mice hair samples. The shaded part refers to the SD of the spectrum. The dotted lines represent the main Raman features observed for melanin.

the values of the extracted features are listed in Tables S1 and S2. Figure S2 indicates that there are differences in the peak positions and bandwidths between the Raman spectra of melanin acquired from 532 and 785 nm. These differences in the Raman spectra highlight the complexity of melanin's molecular structure. The vibrational band assignments for the melanin spectrum at each excitation wavelength are listed in Table S3. Several peaks exhibit noticeable shifts in their positions between the two spectra. The peaks in the 532 nm spectrum are generally narrower compared with those in the 785 nm spectrum. The relative intensities of the peaks vary between the two spectra, further emphasizing the impact of resonance Raman scattering. These observations suggest that the melanin Raman signal exhibits a high degree of sensitivity to the heterogeneity within its chromophores, which respond differently to distinct excitation wavelengths.

Radiation response in melanin at 532 and 785 nm

Melanin spectra from control and irradiated mice hair were converted to second derivatives to resolve the underlying superimposed vibrational features using the Savitzky–Golay algorithm for further analysis (Fig. 2). The second derivative spectra were analyzed to compare the results obtained at 532 and 785 nm excitation wavelengths. This analysis was further extended to compare features of irradiated mice with those of control mice to identify significant Raman frequencies that could be objectively measured and used as reliable biomarkers of radiation exposure and associated physiological changes.

We primarily focused on identifying the main spectral features of melanin and determining the variations in Raman frequencies at both 532 and 785 nm excitation wavelengths. As described in the "Melanin features at 532 and 785 nm" section, notable peak

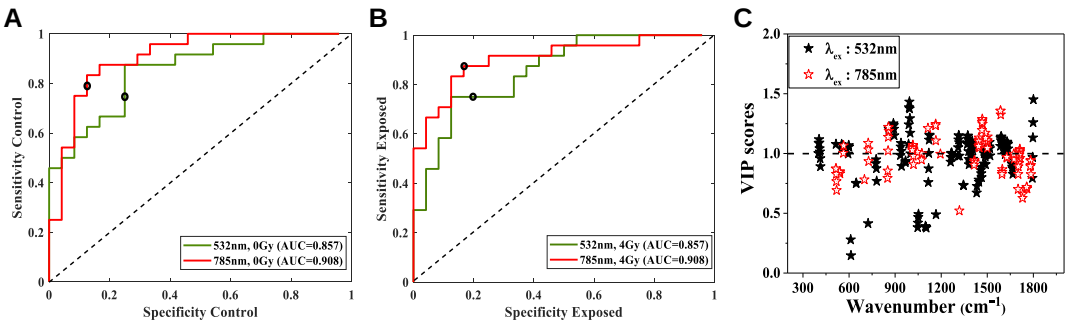

Fig. 3. A comparison of ROC curves representing classification results for 532 nm (green) and 785 nm (red), separating two classes of melanin spectra assigned to A) control and B) gamma-irradiated mice. C) A comparison of VIP scores of the PLS-DA classification models for radiation exposure constructed from melanin spectra at 532 nm (filled black stars) and 785 nm (open red stars) using selected variables.

broadening and frequency shifts occurred at 785 nm compared with 532 nm (Fig. 2), and all Raman band assignments are listed in Table S3. The melanin bands attributed to C–N stretching, C=C stretching, and C–C aromatic within the 1,345–1,606 cm^{-1} region, as well as the C–H deformation band at 979 cm^{-1}, exhibited an ~10 wavenumber shift towards lower frequencies at 785 nm compared with 532 nm. Other melanin bands appeared at their original frequencies but showed a higher intensity relative to the 532 nm spectra.

To assess radiation response in melanin, we first examined the major spectral features of the melanin from mice obtained with 532 nm. An inspection of the features of the melanin from the control and irradiated mice showed negligible changes, and they are nearly superimposed (Fig. 2a and b). They both show typical Raman spectral features of melanin bands at 1,344, 1,409, and 1,523, 1,606cm^{-1}, attributed to the vibrations of C–N, C=C stretching, and the C–C aromatic modes. Other features include the C–H in-plane deformation, N–H in-plane deformation, and C–OH stretching vibrations in the 980–1,200 cm^{-1} spectral region. Further overlapping weak bands attributed to aromatic ring deformation and C–H out-of-plane deformation in the 470–860 cm^{-1} region are observed.

Figure 2c and d represents the second derivative spectra of melanin measured from control and gamma-irradiated mice acquired at 785 nm. The second derivative spectrum of melanin at 785 nm indicated notable spectral alterations between control and gamma-irradiated mice. The observed changes likely occurred within the 1,340–1,596 cm^{-1} spectral region, corresponding to C–N and C=C stretching vibrational modes and C–C aromatic vibrations, with a frequency shift of 2–5 wavenumbers. The dual band attributed to C–N vibration, observed at control samples within the 1,332–1,345 cm^{-1} region, consolidated into a single Raman band at 1,340 cm^{-1} within irradiated mice. The Raman bands observed within the 1,200–1,271 cm^{-1} range, attributed to C–OH and C–O vibrations, respectively, exhibited reduced amplitude postexposure. C–H in-plane deformation band at 1,041 cm^{-1} shows red shift of 6–7 wavenumbers. C–H out-of-plane deformation in 738–890 cm^{-1} appeared to vary in amplitude. The aromatic ring deformation and O=C=O deformation within the COOH group, observed at 541 and 602 cm^{-1}, exhibited a 2-wavenumber shift towards lower frequencies with an increase in amplitude. At 1,693 cm^{-1}, the C=O stretching within COOH group also showed definite changes.

Classification models for triage assessment

To categorize and quantify the mice samples as unexposed or exposed, PLS-DA was applied over the Raman measurements of melanin. For PLS-DA-based triage models, second derivative spectra were split into control (0 Gy) and gamma-irradiated (4 Gy) mice groups. Spectral data from male and female mice hair samples collected at days 1, 7, and 25 postexposure were combined across these two groups for binary classification. When all spectral variables from the fingerprint region were included as input features, PLS-DA classification models lacked the ability to distinguish between classes effectively, resulting in random guessing accuracy. PLS-DA models using LOO and VB cross-validations were constructed to evaluate the model's performance. Table S4 presents statistical metrics for both LOO and VB methods using all spectral features of melanin at 532 and 785 nm.

Table 1. Cross-validation statistics of the PLS-DA models of exposure on the melanin spectra collected at 532 and 785 nm using LOO.

	532 nm		785 nm	
	Unexposed	**Exposed**	**Unexposed**	**Exposed**
Class error (CV)	0.229	0.229	0.145	0.145
Sensitivity (CV)	0.792	0.750	0.833	0.875
Specificity (CV)	0.750	0.792	0.875	0.833
AUC (CV)	0.857	0.857	0.908	0.908
No. of LVs	4	4	5	5

To identify key spectral features in melanin for binary classification, we employed variable selection using the selectivity ratio. Subsequently, PLS-DA triage models were constructed using these features for both 532 and 785 nm data. Model performance was evaluated using ROC curve analysis for LOO cross-validations (Fig. 3A and B). We observed improved ability to distinguish between control and gamma-irradiated mice using key features within melanin spectra. The sensitivity, specificity, and area under the curve (AUC) values, summarized in Table 1, provide a quantitative measure of the model's performance using LOO cross-validation. The PLS-DA model could successfully discriminate the unexposed group from the irradiated groups with a sensitivity of 83% and a specificity of 87% at 785 nm, indicating that the features in the unexposed mice are different from those seen in the exposed groups. Similarly, the PLS-DA model achieved a sensitivity of 79% and specificity of 75% for dose classification at 532 nm. The model's AUC values ranged from 0.85 to 0.91 for 532 and 785 nm, respectively, indicating excellent discrimination between control and irradiated groups.

It is possible to determine which variables are most important in the classification model by evaluating VIP scores. VIP scores quantify each variable's influence on the PLS model, and the typical threshold value is 1 for which VIP scores >1 are considered significant. The VIP scores constructed from PLS-DA classification on

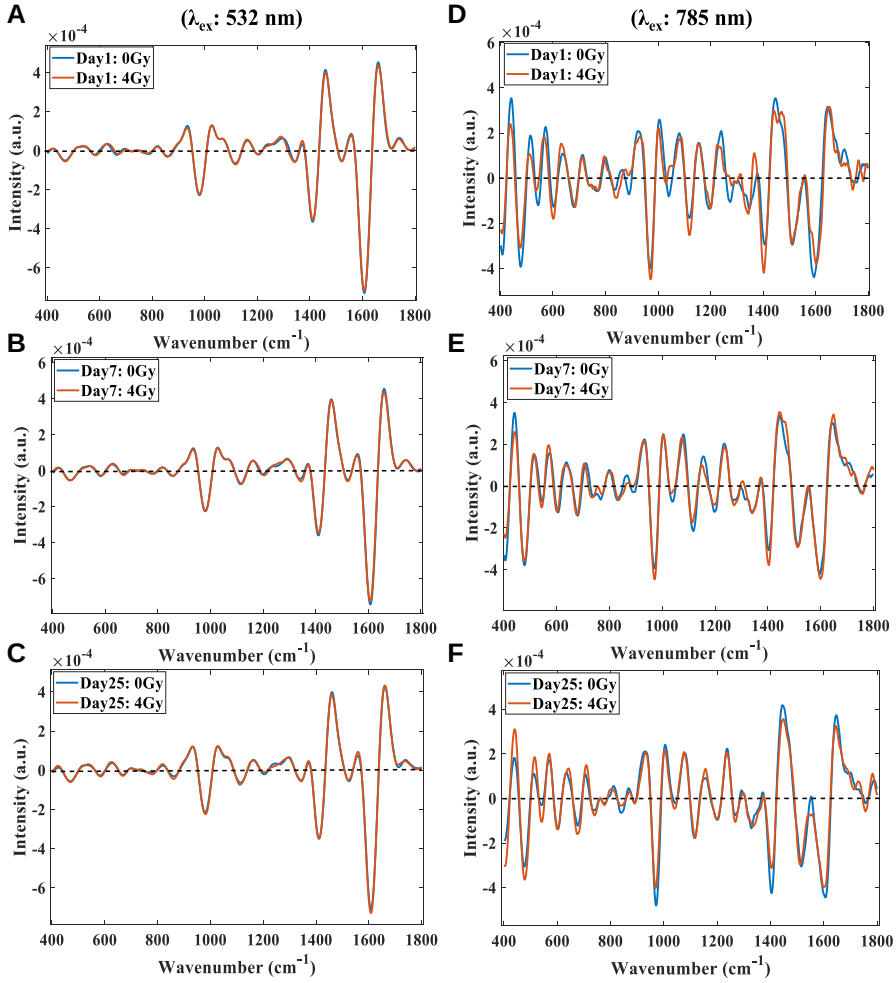

Fig. 4. The mean second derivative spectra of melanin (400–1,800 cm^{-1}) from the control (0 Gy) and gamma-irradiated (4 Gy) mice at 532 nm for A) day 1, B) day 7, C) day 25, and at 785 nm for D) day 1, E) day 7, and F) day 25.

control and gamma-irradiated hair samples for 532 and 785 nm were compared for further analysis (Fig. 3C). The specific variables noted may arise from different electronic resonances probed by the 532 or 785 nm excitation laser, as discussed above.

The spectral regions exhibiting the greatest influence on discrimination at 785 nm are associated with C=C and C–N stretching (1,400–1,500 cm^{-1}), C–H out-of-plane deformation, and N–H in-plane deformation (870–1,116 cm^{-1}) Raman bands. At 532 nm, however, the vibrational modes most weighted and with the greatest influence on the obtained discrimination were associated with C–H in-plane and C=O stretching regions. All PLS-DA models and associated statistical values obtained using VB cross-validation are presented in Fig. S3 and Table S5. VB cross-validation indicated no major differences in classification model performance between 532 and 785 nm data, including identical variable selection to LOO.

Radiation-induced temporal changes in melanin

To quantify time-dependent changes in melanin postexposure and explore the potential of biomarkers for rapid medical triage applications, Raman measurements were analyzed at days 1, 7, and 25 postexposure. Second derivative spectra of melanin were compared for control and gamma-irradiated hair samples for all three time points (Fig. 4). Distinct time-dependent spectral responses were observed between the 532 and 785 nm excitation wavelengths following gamma irradiation.

The 532 nm spectra showed little to no differences between control and irradiated mice across all time points, indicating potential limitations in sensitivity or dosimetry response at this wavelength (Fig. 4A–C). The second derivative spectra acquired at 785 nm demonstrate that nearly all Raman frequencies are sensitive to radiation dose (Fig. 4D–F). Moreover, the intensity of these bands varies across different time points postirradiation, indicating spectral changes evolve over time following radiation exposure.

The PLS-DA classification models were performed using second derivative spectral data at both excitation wavelengths to distinguish between control and irradiated samples at each postexposure time point. The comparison of model's ROC curve for control and exposed mice at 532 and 785 nm is shown in Fig. S4.

The PLS-DA classifications using melanin spectra at 532 and 785 nm can effectively distinguish between control and irradiated mice samples at all three time points. VIP scores for each time point indicate that different spectral regions are necessary for classification at distinct postirradiation intervals (Fig. 5A–C). One day postexposure, C–N and C=C stretching vibrations differentiated healthy and irradiated mice using both 532 and 785 nm lasers. After a week, 785 nm spectra emphasized aromatic rings, C–H out-of-plane, N–H, and C–N stretching, while 532 nm

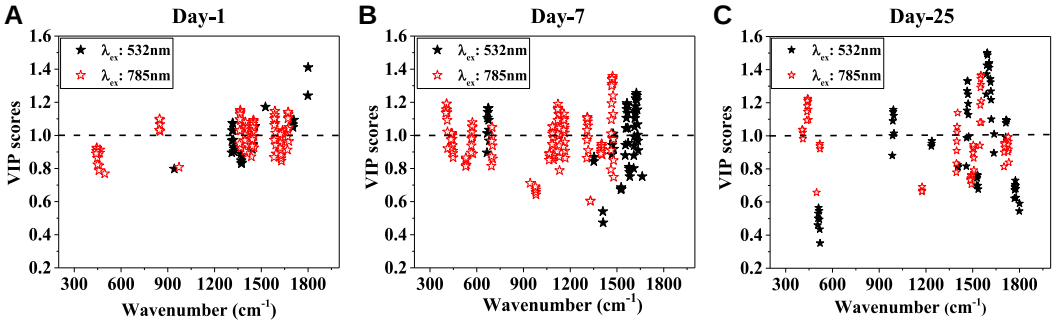

Fig. 5. A comparison of VIP scores of the PLS-DA models for radiation exposure constructed from 532 nm (filled black stars) and 785 nm (open red stars) melanin spectra at A) day 1, B) day 7, and C) day 25, postexposure. The black dotted line shows the significance threshold.

classified on C=C aromatic ring deformation band. At 25 days, 785 nm continued to highlight aromatic rings and C–N stretching, with some C=C contribution, while 532 nm primarily used C=C and C–H in-plane deformation. However, a closer examination of statistical metrics at both excitation wavelengths is necessary to validate these findings (Table S6). The time-dependent decrease in AUC values observed in ROC curves over time at both wavelengths further emphasizes the alterations in melanin spectral characteristics following radiation exposure. The PLS-DA classification using 785 nm spectral data demonstrated exceptional performance, with minimal classification errors achieving perfect sensitivity and specificity (100%) for differentiating healthy and irradiated mice at all time points except day 25 (88%). Moreover, the PLS-DA models at 532 nm exhibited relatively higher classification errors with poor sensitivity and specificity, suggesting overfitting or the model's limitation in capturing the complexity of the data.

A comparison of VIP scores plots from PLS-DA models constructed using VB cross-validation at 532 and 785 nm spectral data at three different time points are shown in Fig. S5. Associated statistical values obtained using VB cross-validation are tabulated in Table S7. VB cross-validation indicated more or less similar classification and statistical values between 532 and 785 nm data, compared with LOO.

Prediction of time postexposure

PLSR models were developed to predict time postexposure based on second derivative spectra of melanin within the fingerprint region (400–1,800 cm^{-1}). Initially, we attempted to develop prediction models with all spectral variables in melanin spectra, considering all three technical replicates from each mouse sample (total spectra, $n = 144$). PLSR models using leave-LOO and VB cross-validations were constructed to evaluate the model's performance. Employing spectra without averaging technical replicates leads to substantial biological variability in the data, compromising the model's performance with both cross-validation methods employed. Models were evaluated using data acquired at both 532 and 785 nm excitation wavelengths, and corresponding parity plots are shown in Figs. S6 and S7. Figure S8 illustrates a comparison of VIP scores for PLS models constructed using 532 and 785 nm spectral data. A comparison of VIP scores obtained through both LOO and VB cross-validation (Fig. S8A and B) indicates that PLS models are influenced by the all the variables in the spectra.

To mitigate biological variability in the models, technical replicates were averaged to create a single representative spectrum for each sample, and prediction models were rebuilt using PLSR on reduced data size ($n = 48$). A comparison of PLS model performance between 532 and 785 nm data was conducted using both LOO and VB cross-validations, and parity plots are shown in Figs. S9 and S10. Corresponding VIP scores for these models at 532 and 785 nm are shown in Fig. S11A and B. Interestingly, despite reducing spectral complexity through averaging technical replicates, PLS models continued to be influenced by the same melanin spectral features, as highlighted by VIP scores in Figs. S8 and S11 and consequently exhibited poor performance.

Table S8 summarizes the model's performance metrics at both excitation wavelengths for LOO and VB cross-validations. The table provides R^2 and RMSE values and the recommended number of LVs based on cross-validation results. The statistical metrics from PLSR analysis demonstrate that utilizing all spectral variables without averaging technical replicates led to suboptimal performance of the PLS models for both excitation wavelengths. The R^2 and RMSE values for these models were unsatisfactory for both LOO and VB validation methods. Model performance did not improve after averaging technical replicates, showing the model's limitations. This is attributed to the models consistently focusing on the same spectral features, as shown in VIP scores in Figs. S8 and S11. The consistent selection of only one LV further emphasizes the model's inability to capture the complexity of the data.

In our next step, we employed a variable selection step prior to developing PLS models to identify the most significant features in spectral regions contributing to the model. Variable selection in PLS analysis is necessary to identify the most relevant predictors from a large variable set and improve the accuracy of prediction models (40–42). Selecting key melanin features within the fingerprint region further improved prediction models and calibration for both 532 and 785 nm excitation wavelengths. Figure 6A and B shows cross-validation parity plots illustrating measured and predicted time points based on selected melanin features at 532 and 785 nm excitation, respectively. Using LOO cross-validation, PLSR models resulted in two or more LVs, which accounted for the complexity of the data considering sex, dose, and age factors. Table S9 summarizes the PLSR model's performance metrics for both excitation wavelengths. The RMSE for PLSR models is ~9 days and an R^2 of 0.1 when using three technical replicates per mouse as input features. Reducing biological variation with selected key features in melanin improved both R^2 and RMSE values for both laser wavelengths, with more significant enhancements observed at 785 nm. The PLS model for time point prediction yielded an R^2 of 0.5 and an RMSE of ~7 days for 785 nm. For 532 nm, the PLS model with two LVs resulted in an R^2 of 0.3 and an RMSE of ~8.6 days.

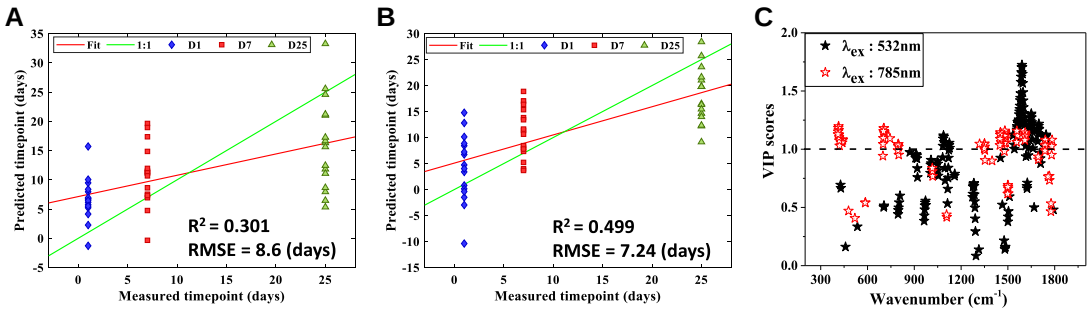

Fig. 6. Cross-validation parity plots showing the estimated time points versus the true time points using PLSR with selected spectral variables in melanin at A) 532 nm and B) 785 nm. Cross-validation was performed using the LOO method. C) A comparison of VIP scores of the PLSR models time from exposure constructed from 532 nm (filled black stars) and 785 nm (open red stars) with selected melanin features.

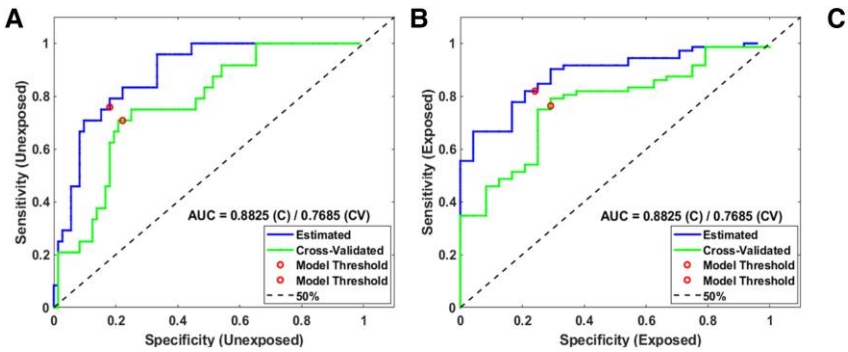

C

N=96	Predicted		
Actual	Classes	Exposed	Unexposed
	0 Gy	TP=17	FN=7
	1 Gy	TN=18	FP=6
	2 Gy	TN=18	FP=6
	4 Gy	TN=19	FP=5

Fig. 7. ROC curves representing classification results for 785 nm, separating two classes of melanin spectra assigned to A) unexposed (0 Gy) and B) gamma-irradiated mice (1, 2, and 4 Gy combined). C) A table constructed from cross-validation of classification model summarizes predicted class labels to the actual class labels.

The comparison of VIP scores constructed for 532 and 785 nm is shown in Fig. 6C. Interestingly, both excitation wavelengths interacted with melanin differently, leading to distinct feature selection in PLSR prediction models. This finding is consistent with the different levels of sensitivity of laser wavelengths towards chromophores in melanin, as discussed above. The 532 nm wavelength predominantly captured spectral information associated with C–N and C=C stretching vibrations within the 1,350–1,700 cm^{-1} region, with a minor contribution from N–H deformation at 1,120 cm^{-1}. However, the 785 nm wavelength was sensitive to C–N, C=C, and C=O stretching vibrations within the (1,320–1,750 cm^{-1}), aromatic ring structures (415 cm^{-1}), and C–H deformations, primarily within 670–780 cm^{-1} spectral ranges.

Similarly, parity plots were constructed using VB cross-validation, and results are shown in Fig. S12A and B. VB analysis showed similar but differently weighted variable selection in VIP scores for each excitation wavelength (Fig. S12C), emphasizing the distinct characteristics of both excitation wavelengths towards melanin. Table S10 provides the statistical analysis for PLS models using VB cross-validation at both excitation wavelengths. LOO cross-validation was selected, as it simulates the way the model might be deployed to real samples in which all of these data are collected to train a model, and then a single sample is presented to the model independently for a time point or triage. In this study, LOO analysis shows stronger results, although VB cross-validation exhibited similar RMSE. VB cross-validation (see Supplementary Material) was also utilized to check against overestimates of model performance in large sample sizes previously reported with LOO cross-validation (43–46).

Triage model and dose estimation for extended dosages using 785 nm

Based on our observation that 785 nm excitation demonstrated better sensitivity compared with 532 nm, we focused our extended dosage study exclusively on the 785 nm excitation wavelength. To evaluate the proposed method's ability to differentiate between low- and high-dose irradiated samples, a PLS-DA model was developed utilizing Raman spectra of pigment collected at a 785-nm wavelength to classify unexposed mice and those exposed to various radiation dosages (1, 2, and 4 Gy). The performance of this classification model is illustrated by the ROC curves presented in Fig. 7A and B. The model demonstrates a sensitivity of 75% and a specificity of 78%, suggesting a moderate capacity to distinguish between unexposed (0 Gy) and exposed (1, 2, and 4 Gy, combined) cases. These metrics indicate that the model has comparable efficacy in identifying both irradiated and nonirradiated samples.

The table in Fig. 7C shows balanced classes with similar true and false rates for each dose, indicating the model's performance is consistent across different radiation levels. This balance indicates that the model does not have a strong bias towards any particular dose, including the ability to differentiate between lower and higher doses.

To evaluate the model's discrimination ability between distinct dose levels (0 versus 1, 2, and 4 Gy), supplementary classification

models were developed. The performance metrics of these additional models are presented in Table 2. These results demonstrate that the proposed method effectively differentiates between unexposed and exposed mice and those who were exposed with lower (0 + 1 Gy) versus higher dose (2 + 4 Gy) levels. The cross-validation statistics reveal a progressive improvement in sensitivity as the radiation dose increases. This trend indicates moderate sensitivity for detecting low-dose radiation exposure (1 Gy) and progressively better sensitivity for higher doses (2 and 4 Gy).

Further, dose-prediction analysis was conducted to assess the uncertainty in radiation dosage estimates at various time points postexposure. Figure 8 presents parity plots illustrating the relationship between predicted and actual dosages at different time intervals following irradiation across various dose levels. The statistical significance of the regression models for individual time points was evaluated using a permutation test. The results demonstrate that these models are statistically significant at the 95% confidence level. The corresponding cross-validation metrics for these predictions are detailed in Table 3.

As shown in Table 3, when all time points are combined, the uncertainty in dose prediction exceeds 1 Gy. However, when regression analysis is performed for individual time intervals of days 1, 7, and 25, the uncertainty in dose prediction decreases to >1 Gy. This observation is consistent with our data above, which indicated that models incorporating information about the time elapsed since exposure yield improved exposure predictions.

Table 2. Cross-validation statistics of the PLS-DA models on the melanin spectra collected from varying dosages using 785 nm.

	Exposure status	Sensitivity	Specificity	AUC	Class error
0 vs. 1 + 2 + 4 Gy	Unexposed	0.750	0.778	0.768	0.236
	Exposed	0.778	0.750	0.768	0.236
0 + 1 vs. 2 + 4 Gy	Unexposed	0.750	0.750	0.794	0.250
	Exposed	0.750	0.750	0.794	0.250
0 vs. 1 Gy	Unexposed	0.750	0.708	0.748	0.270
	Exposed	0.708	0.750	0.748	0.270
0 vs. 2 Gy	Unexposed	0.792	0.833	0.895	0.187
	Exposed	0.833	0.792	0.895	0.187
0 vs. 4 Gy	Unexposed	0.833	0.875	0.908	0.145
	Exposed	0.875	0.833	0.908	0.145

Discussion

Melanin plays a crucial role in radiation dosimetry due to its involvement in various physiological processes and ability to absorb and scatter radiation (9, 47). Understanding melanin's response to ionizing radiation is essential, as it offers potential as a biomarker for radiation exposure and can elucidate the underlying mechanisms of radiation-induced damage (8). Here, we have employed Raman spectroscopy to identify the unique spectral signatures of melanin from the hair samples of relatively low-dose gamma-irradiated C57BL/6 mice and not cause significant cutaneous radiation syndromes (CRSs). We utilized dual excitation wavelengths of 532 and 785 nm to identify the distinctive melanin features and explored radiation-induced changes that could serve as promising biomarkers.

The distinct sensitivity of the two excitation wavelengths to gamma radiation was investigated using second derivative spectra of melanin. Melanin spectra obtained from hair samples of control and gamma-irradiated mice show visually imperceptible differences in Raman characteristics at 532 nm (Fig. 2a and b). Gamma irradiation may induce changes at a molecular level that do not drastically alter the overall spectrum but affect specific features used for classification (48). Our findings indicate notable spectral changes in melanin for irradiated hair samples compared with control mice with a 785-nm excitation wavelength. The amplitude and position of the Raman bands changed, enabling the characterization of radiation-induced alterations in melanin at 785 nm (Fig. 2c and d). The more pronounced response to gamma irradiation at 785 nm is likely due to the preferential interaction with larger chromophores. The longer conjugation length of the 785 nm excitation chromophore may be more susceptible to disruption by radical formation than at 532 nm, which would explain the greater sensitivity to radiation damage. These larger chromophores are more susceptible to radiation-induced changes, including radical formation and melanin aggregation (11, 13, 14, 30). These effects are more apparent in the spectral response of larger chromophores, which demonstrates the more noticeable spectral changes observed at 785 nm compared with 532 nm excitation. The chemical bonds most susceptible to these radiation-induced transformations seem primarily to be those constituting the extended conjugated systems within these larger melanin subunits. These include C–C bonds in aromatic rings, C–N vibrations in indole-like moieties, C–H vibrations, and C–O bonds in quinone structures, and aromatic ring deformations within the spectral regions of 1,340–1,596, 1,200–1,271, 1,041–738, 602, and 541 cm^{-1}, respectively, at 785 nm (Table S3).

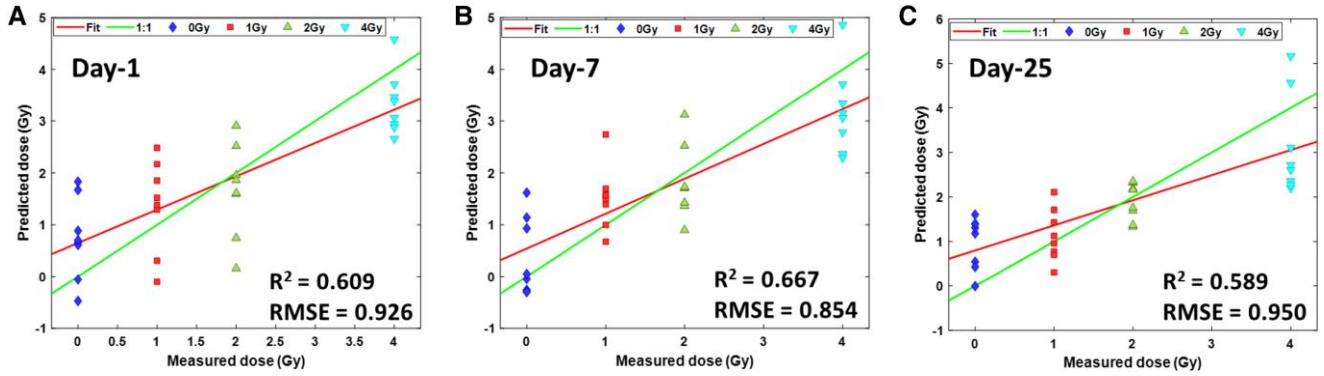

Fig. 8. Cross-validation parity plots show the estimated dosages versus the true dosages of 0, 1, 2, and 4 Gy for individual time points of A) day 1, B) day 7, and C) day 25, using melanin spectra collected at 785 nm.

Table 3. Validation statistics of the PLSR models for dose estimation on the melanin spectra collected at 785 nm.

Time points	No. of LVs	R^2	RMSE
All time points combined	4	0.571	1.365
Day 1	4	0.609	0.926
Day 7	4	0.667	0.854
Day 25	4	0.589	0.950

To evaluate the potential of Raman spectroscopy as a tool for rapid medical triage in radiation exposure scenarios, we employed PLS-DA classification. PLS-DA models were developed to distinguish between healthy mice and those exposed to a relatively low dose (4 Gy) of gamma radiation. The ROC analysis demonstrates that the PLS-DA models derived from second derivative spectra of melanin achieved optimal performance in classifying between healthy and gamma-irradiated mice (Fig. 3A and B). Validation statistics from models achieved better classification at 785 nm excitation, with a sensitivity of 83%, specificity of 87%, compared with 532 nm, which showed a sensitivity of 79% and specificity of 75% (Table 1). The model's AUC values ranged from 0.85 to 0.91 for 532 and 785 nm, respectively, indicating excellent discrimination between control and irradiated groups. The VIP score analysis shows that radiation-induced changes in melanin's molecular structure are associated to specific chemical bonds in the spectral regions of 1,400–1,500 cm^{-1} (C=C and C–N stretching) and 870–1,116 cm^{-1} (C–H and N–H vibrations) for 785 nm, yet they are not prominently observed at 532 nm (as illustrated in Fig. 3C). The inferior performance of classification models based on 532 nm melanin spectra may be due to 532 nm excitation probing smaller conjugation length chromophores (28, 29, 49, 50) which have less probability of being disrupted by radiation-induced damage. Further, triage models based on the 785 nm spectral data showed the ability to discriminate between mice unexposed and those exposed to varying levels of gamma radiation (1, 2, and 4 Gy; Fig. 7 and Table 2). These triage models effectively differentiated between lower (0 + 1 Gy) versus higher (2 + 4 Gy) dose levels, demonstrating the ability to distinguish between different levels of radiation exposure.

Other attempts to perform retrospective dosimetry using hair have utilized electron spin resonance (ESR) spectroscopy (51). It has been shown that decay of ESR signal varies with hair color, implying that the radical signal generated by radiation exposure quenches at time dependent on the type of pigmentation present (52–54). ESR signals for black hair in humans from high doses gamma-ray exposure (12 kGy) reached 50% signal intensity within 44-h postexposure, implying that radiation-induced radicals are quenched—either through damage or recombination—within about a week postexposure (52). Unfortunately, due to strong overlapping background signals from melanin and other components of hair, ESR is not expected to be appropriate for medical triage at or below doses of about 2 Gy (52), while our results indicate Raman can work at lower doses.

The time-dependent changes in melanin spectra following radiation exposure indicate the potential of Raman biomarkers for rapid medical triage applications. Given that the hair growth cycle in mice typically spans 3–4 weeks (55), the measured time points of days 1, 7, and 25 postexposure provide an ideal framework for studying radiation-induced effects. Analysis of second derivative spectra of melanin in control and gamma-irradiated hair samples across all three time points demonstrated melanin's sensitivity to 4 Gy when excited at 785 nm, showing more pronounced spectral changes compared with 532 nm excitation (as shown in Fig. 4). The PLS-DA classifications utilizing melanin spectra obtained at 785 nm excitation demonstrated exceptional performance in differentiating between control and irradiated mice samples across all three time points. The ROC analysis achieved excellent results, yielding perfect sensitivity and specificity (100%) for days 1 and 7, with a light decrease in performance, but still maintaining a robust sensitivity of 100% and specificity of 88% at day 25. The time-dependent decline in AUC values observed in ROC curves for the 785 nm wavelength further emphasizes the significant alterations in melanin spectral characteristics postradiation exposure (Table S6). Analysis of VIP scores for each time point revealed that distinct spectral regions play critical roles in classification at different postirradiation intervals (Fig. 5A–C). Our dose-prediction model revealed statistically significant regression models at different time points postexposure (Fig. 8 and Table 3). Combining all time points resulted in dose-prediction uncertainty >1 Gy, but analyzing individual time intervals (days 1, 7, and 25) reduced uncertainty to <1 Gy. The changing spectral features over time imply that melanin acts as a dynamic biomarker, potentially reflecting different stages of cellular response to gamma irradiation damage and repair processes. The changes in melanin features may be associated with depigmentation response associated with radiation-induced cell damage (11, 56, 57). It may be beneficial for biodosimetry applications to develop models that incorporate spectral changes at multiple time points to provide a more comprehensive assessment of radiation exposure and its downstream biological effects. The temporal analysis allowed us to track the evolution of melanin's spectral characteristics and evaluate their efficacy as indicators of radiation exposure over time. Although 4 Gy gamma ray may not cause significant damage to the skin epithelium leading to CRS, when exposed to the whole body will result in significant hematopoietic acute radiation syndrome (H-ARS) in mice as well as humans, manifested within days after exposure. Thus, the radiation dose and time points tested in the current study are relevant for triage and clinical decision-making following a nuclear event.

Our results suggest the chemical changes to the melanin pigment evolve with time following exposure to ionizing radiation. We employed machine learning algorithms to construct predictive models capable of estimating time postexposure from second derivative spectral data. Our PLSR models demonstrated different predictive capabilities and calibration accuracy for both 532 and 785 nm excitation wavelengths (Fig. 6A and B). When incorporating three technical replicates per mouse as input features, the models achieve an RMSE of ~9 days. However, this accuracy is further enhanced to an RMSE of ~7 days after determining a single representative spectrum from each mouse sample. Individual mice, even from inbred strains, can exhibit biological variability in terms of gene expression and metabolic profiles (58). Determining a representative spectrum from each mouse sample (e.g. the average from multiple hairs from a mouse) helped focus on the core biological signal rather than intrinsic biological variation. The improved RMSE suggests that using the average spectrum effectively reduces noise and captures the most relevant spectral features associated with radiation-induced changes in melanin. The VIP scores help identify the most important spectral regions that contribute to the performance of the model. As discussed above, the melanin response varied significantly between the two excitation wavelengths, leading to the selection of distinct melanin features in the VIP scores from PLSR prediction models (Fig. 6C). This result not only validates the sensitivity of our Raman spectroscopy–based method but also highlights its

potential as a noninvasive tool for retrospective radiation dose assessment in biological systems.

Conclusion

Noninvasive techniques for retrospective detection of radiation exposure offer significant potential to enhance current biological dosimetry practices, offering more efficient and accurate approaches to assessing radiation exposure in various scenarios. Raman spectroscopy effectively detects radiation-induced melanin changes, enabling rapid, noninvasive identification of low-dose radiation exposure over time. In this study, hair samples from mice exposed to 4 Gy gamma irradiation were measured by Raman spectroscopy to determine the radiation-induced changes in melanin Raman spectra. Our findings indicate that 785 nm excitation is more sensitive to radiation-induced changes in melanin compared with 532 nm excitation, which is a critical factor for use in biodosimetry. This suggests that longer wavelengths are more effective for detecting structural modifications in larger melanin units that are more susceptible to radiation damage. The enhanced sensitivity of our models, particularly with 785 nm excitation, shows that Raman spectroscopy could detect subtle changes as low as 1 Gy and possibly at even lower radiation doses. The ability to discriminate exposure above 2 Gy from lower exposure could be key in effectively triaging patients for ARS following radiation accidents. The identification of specific spectral regions (1,400–1,500 and 870–1,116 cm^{-1}) associated with radiation-induced changes provides candidate Raman biomarkers for biological biodosimetry. These markers, linked to C=C, C–N, C–H, and N–H vibrations, offer a molecular-level insight into radiation effects on melanin. Our investigation of time-dependent changes in melanin spectra following radiation exposure is particularly relevant for rapid triage applications. This approach aligns with the need for quick assessment methods in emergency situations involving radiation exposure. The ability to detect spectral changes correlated with radiation exposure suggests the potential for noninvasive quantitative models to estimate radiation dose, which is crucial for triage, clinical decision-making and treatment applications.

Acknowledgments

The authors acknowledge the use of the Small Animal Imaging Core (SAIC) Shared Resource at The Ohio State University Comprehensive Cancer Center – Arthur G. James Cancer Hospital and Richard J. Solove Research Institute, Columbus, OH, USA.

Supplementary Material

Supplementary material is available at *PNAS Nexus* online.

Funding

This research was supported by the Intelligence Advanced Research Projects Activity (IARPA) TEI-REX program through the Army Research Office contract W911NF-22-2-0140. The views and conclusions contained should not be interpreted as necessarily representing the official policies, either expressed or implied, of ODNI, IARPA, ARO, or the US government. The US government is authorized to reproduce and distribute reprints for governmental purposes notwithstanding any copyright annotation therein. The SAIC Shared Resource at The Ohio State University Comprehensive Cancer Center – Arthur G. James Cancer Hospital and Richard J. Solove Research Institute is partly supported by National Cancer Institute core grant P30CA016058.

Author Contributions

Monika Poonia (Conceptualization, Data curation, Formal analysis, Investigation, Methodology, Writing—original draft), Spencer A. Witte (Data curation, Formal analysis, Methodology, Writing—review & editing), Mallard Woodward (Data curation, Investigation, Writing—review & editing), Prasant Yadav (Resources, Writing—review & editing), Sapna Puri (Resources, Writing—review & editing), Ramasamy Santhanam (Resources, Writing-review & editing), Naduparambil K. Jacob (Conceptualization, Funding acquisition, Project administration, Resources, Supervision, Writing-review & editing), Zachary D. Schultz (Conceptualization, Data curation, Formal analysis, Funding acquisition, Methodology, Project administration, Resources, Supervision, Writing—review & editing).

Data Availability

The Raman data used in this work is available at Zenodo.org (https://doi.org/10.5281/zenodo.14900547) (59).

References

1 Song W, *et al.* 2023. Melanin: insights into structure, analysis, and biological activities for future development. *J Mater Chem B*. 11(32):7528–7543.
2 Ilina A, *et al.* 2022. The photoprotection mechanism in the black–brown pigment eumelanin. *Proc Natl Acad Sci U S A*. 119(43): e2212343119.
3 Guo L, *et al.* 2023. Recent advances and progress on melanin: from source to application. *Int J Mol Sci*. 24(5):4360.
4 Wakamatsu K, Ito S. 2023. Recent advances in characterization of melanin pigments in biological samples. *Int J Mol Sci*. 24(9):8305.
5 Fernandes B, Cavaco-Paulo A, Matamá T. 2023. A comprehensive review of mammalian pigmentation: paving the way for innovative hair colour-changing cosmetics. *Biology (Basel)*. 12(2):290.
6 Wang X, *et al.* 2023. Indole-5,6-quinones display hallmark properties of eumelanin. *Nat Chem*. 15(6):787–793.
7 Mosse I, *et al.* 2000. Melanin decreases clastogenic effects of ionizing radiation in human and mouse somatic cells and modifies the radioadaptive response. *Radiat Environ Biophys*. 39(1):47–52.
8 Matsumoto K-I, *et al.* 2020. Effects of low-dose X-ray irradiation on melanin-derived radicals in mouse hair and skin. *J Clin Biochem Nutr*. 67(2):174–178.
9 Brenner M, Hearing VJ. 2008. The protective role of melanin against UV damage in human skin†. *Photochem Photobiol*. 84(3):539–549.
10 Zamudio Díaz DF, *et al.* 2024. Significance of melanin distribution in the epidermis for the protective effect against UV light. *Sci Rep*. 14(1):3488.
11 Ungvari A, *et al.* 2024. Irradiation-induced hair graying in mice: an experimental model to evaluate the effectiveness of interventions targeting oxidative stress, DNA damage prevention, and cellular senescence. *GeroScience*. 46(3):3105–3122.
12 Reisz JA, *et al.* 2014. Effects of ionizing radiation on biological molecules—mechanisms of damage and emerging methods of detection. *Antioxid Redox Signal*. 21(2):260–292.
13 Abd El-Azeem SA, Alajmi AM. 2024. Study of the effect of gamma rays on the melanin physical properties and its release from liposomes. *Arab J Sci Eng*. 49(1):1141–1150.

14 Dadachova E, *et al.* 2007. Ionizing radiation changes the electronic properties of melanin and enhances the growth of melanized fungi. *PLoS One*. 2(5):e457.
15 Turick CE, *et al.* 2011. Gamma radiation interacts with melanin to alter its oxidation–reduction potential and results in electric current production. *Bioelectrochemistry*. 82(1):69–73.
16 Castelvecchi D. 2007. Dark power: pigment seems to put radiation to good use. *Sci News*. 171(21):325.
17 Tran ML, Powell BJ, Meredith P. 2006. Chemical and structural disorder in eumelanins: a possible explanation for broadband absorbance. *Biophys J*. 90(3):743–752.
18 Nofsinger JB, Ye T, Simon JD. 2001. Ultrafast nonradiative relaxation dynamics of eumelanin. *J Phys Chem B*. 105(14):2864–2866.
19 Yakimov BP, *et al.* 2020. Melanin distribution from the dermal–epidermal junction to the stratum corneum: non-invasive in vivo assessment by fluorescence and Raman microspectroscopy. *Sci Rep*. 10(1):14374.
20 Galván I, Jorge A. 2015. Dispersive Raman spectroscopy allows the identification and quantification of melanin types. *Ecol Evol*. 5(7):1425–1431.
21 Wilkinson EL, *et al.* 2022. Fingerprinting of skin cells by live cell Raman spectroscopy reveals melanoma cell heterogeneity and cell-type-specific responses to UVR. *Exp Dermatol*. 31(10):1543–1553.
22 Wang H, *et al.* 2016. In vivo coherent Raman imaging of the melanomagenesis-associated pigment pheomelanin. *Sci Rep*. 6(1):37986.
23 Galván I, *et al.* 2013. Raman spectroscopy as a non-invasive technique for the quantification of melanins in feathers and hairs. *Pigment Cell Melanoma Res*. 26(6):917–923.
24 Dodo K, Fujita K, Sodeoka M. 2022. Raman spectroscopy for chemical biology research. *J Am Chem Soc*. 144(43):19651–19667.
25 Raman CV, Krishnan KS. 1928. A new type of secondary radiation. *Nature*. 121(3048):501–502.
26 Qi Y, *et al.* 2024. Applications of Raman spectroscopy in clinical medicine. *Food Front*. 5(2):392–419.
27 Wu W, Ranasinghe JC, Chatterjee A, Huang S. 2024. Recent advances on Raman spectroscopy of graphene: towards biosensing applications. *Mater Chem Phys*. 318:129281.
28 Huang Z, *et al.* 2004. Raman spectroscopy of in vivo cutaneous melanin. *J Biomed Opt*. 9(6):1198.
29 Kohl FR, Grieco C, Kohler B. 2020. Ultrafast spectral hole burning reveals the distinct chromophores in eumelanin and their common photoresponse. *Chem Sci*. 11(5):1248–1259.
30 Lam SE, *et al.* 2021. Raman and photoluminescence spectroscopy analysis of gamma irradiated human hair. *Sci Rep*. 11(1):7939.
31 Dong H, *et al.* 2017. Melanin-associated synthesis of SERS-active nanostructures and the application for monitoring of intracellular melanogenesis. *Nanomaterials*. 7(3):70.
32 Bradley DA, *et al.* 2019. Raman spectroscopy and X-ray photospectroscopy analysis of graphite media irradiated at low doses. *Appl Radiat Isot*. 147:105–112.
33 Weiss TJ, *et al.* 2023. Cell-intrinsic melanin fails to protect melanocytes from ultraviolet-mutagenesis in the absence of epidermal melanin. *Pigment Cell Melanoma Res*. 36(1):6–18.
34 Slominski A, *et al.* 2005. Preservation of eumelanin hair pigmentation in proopiomelanocortin-deficient mice on a nonagouti (a/a) genetic background. *Endocrinology*. 146(3):1245–1253.
35 Tobin DJ. 2008. Human hair pigmentation—biological aspects. *Int J Cosmet Sci*. 30(4):233–257.
36 Solano F. 2020. Photoprotection and skin pigmentation: melanin-related molecules and some other new agents obtained from natural sources. *Molecules*. 25(7):1537.
37 Galván I, *et al.* 2018. Raman spectroscopy quantification of eumelanin subunits in natural unaltered pigments. *Pigment Cell Melanoma Res*. 31(6):673–682.
38 Brandt NN, Brovko OO, Chikishev AY, Paraschuk OD. 2006. Optimization of the rolling-circle filter for Raman background subtraction. *Appl Spectrosc*. 60(3):288–293.
39 Savitzky A, Golay MJE. 1964. Smoothing and differentiation of data by simplified least squares procedures. *Anal Chem*. 36(8):1627–1639.
40 Consonni V, *et al.* 2021. A MATLAB toolbox for multivariate regression coupled with variable selection. *Chemometr Intell Lab Syst*. 213:104313.
41 Mehmood T, Liland KH, Snipen L, Sæbø S. 2012. A review of variable selection methods in partial least squares regression. *Chemometr Intell Lab Syst*. 118:62–69.
42 Farrés M, *et al.* 2015. Comparison of the variable importance in projection (VIP) and of the selectivity ratio (SR) methods for variable selection and interpretation. *J Chemom*. 29(10):528–536.
43 Wong T-T. 2015. Performance evaluation of classification algorithms by k-fold and leave-one-out cross validation. *Pattern Recognit*. 48(9):2839–2846.
44 Jiang G, Wang W. 2017. Error estimation based on variance analysis of k-fold cross-validation. *Pattern Recognit*. 69:94–106.
45 Kim J-H. 2009. Estimating classification error rate: repeated cross-validation, repeated hold-out and bootstrap. *Comput Stat Data Anal*. 53(11):3735–3745.
46 Rodríguez-Pérez R, Fernández L, Marco S. 2018. Overoptimism in cross-validation when using partial least squares-discriminant analysis for omics data: a systematic study. *Anal Bioanal Chem*. 410(23):5981–5992.
47 ElObeid AS, *et al.* 2017. Pharmacological properties of melanin and its function in health. *Basic Clin Pharmacol Toxicol*. 120(6):515–522.
48 Fujita H, Watanabe TM. 2024. Use of optical techniques to evaluate the ionizing radiation effects on biological specimens. *J Radiat Res*. 65(Supplement_1):i117–i125.
49 Ferrari AC, Robertson J. 2000. Interpretation of Raman spectra of disordered and amorphous carbon. *Phys Rev B*. 61(20):14095–14107.
50 Ferrari AC, Rodil SE, Robertson J. 2003. Interpretation of infrared and Raman spectra of amorphous carbon nitrides. *Phys Rev B*. 67(15):155306.
51 Brady JM, Aarestad NO, Swartz HM. 1968. In vivo dosimetry by electron spin resonance spectroscopy. *Health Phys*. 15(1):43–47.
52 Tepe Çam S, Polat M, Seyhan N. 2014. The use of human hair as biodosimeter. *Appl Radiat Isot*. 94:272–281.
53 Kudynski R, Kudynska J, Buckmaster HA. 1994. The decay constant for irradiated human hair using EPR spectroscopy. *Appl Radiat Isot*. 45(6):645–650.
54 Çolak Ş, Özbey T. 2011. An ESR study on biological dosimeters: human hair. *Radiat Meas*. 46(5):465–472.
55 Lin X, Zhu L, He J. 2022. Morphogenesis, growth cycle and molecular regulation of hair follicles. *Front Cell Dev Biol*. 10:899095.
56 Sugaya K, Hirobe T. 2014. Exposure to gamma-rays at the telogen phase of the hair cycle inhibits hair follicle regeneration at the anagen phase in mice. *Int J Radiat Biol*. 90(2):127–132.
57 Hance RT, Murphy JB. 1926. Studies on X-ray effects: xv. The prevention of pigment formation in the hair follicles of colored mice with high voltage X-ray. *J Exp Med*. 44(3):339–342.
58 Wade CM, Daly MJ. 2005. Genetic variation in laboratory mice. *Nat Genet*. 37(11):1175–1180.
59 Poonia M, *et al.* Data Set: Raman Investigation of in Vivo Radiation Exposure on Melanin in Murine Hair. Zenodo, April 2, 2025. https://doi.org/10.5281/zenodo.14900547